J. Fluid Mech. (2001), *vol.* 431, *pp.* 323–345. Printed in the United Kingdom

On the structure and formation of spiral Taylor–Görtler vortices in spherical Couette flow

By WEIMING SHA† AND KOICHI NAKABAYASHI

Department of Mechanical Engineering, Nagoya Institute of Technology, Gokiso-Cho, Showa-Ku, Nagoya, 466-8555, Japan

(Received 1 June 1998 and in revised form 10 September 2000)

A direct numerical simulation of the spherical Couette flow between two spheres with the inner sphere rotating was performed to investigate the detailed structure, formation process and mechanism of the spiral Taylor–Görtler (TG) vortices. For comparison with our previous experiments, a moderate gap case with clearance ratio $\beta = 0.14$ is chosen in the present numerical study. With adequate initial and boundary conditions, we have sucessfully simulated the supercritical spiral TG vortex flow in this system. Analysis of the numerical results reveals the structure and features of the spiral TG vortices. The flow consists of one toroidal TG vortex, one toroidal vortex cell, three spiral TG vortices and a secondary flow circulation in each hemisphere, and this supercritical flow solution features rotational and equatorial asymmetries. It is found that the spiral TG vortices are composed of a pair of counter-rotating, unequal spiral vortices with essentially different structural forms. One begins in the secondary flow circulation at higher latitude and ends with a connection to the toroidal vortex cell at lower latitude while the other one starts on the inner rotating spherical surface at lower latitude and ends on the outer stationary spherical surface at higher latitude. Through sucessive visualizations which display the transient features of the spiral TG vortices, we observe that vortex tearing, splitting, tilting, reconnecting, stretching and compressing occur in the formation of the spiral TG vortices. Pairing of two alternating helical vortices is the key process in their evolution. To understand the formation mechanism, we consider the vorticity production in the azimuthal vorticity component equation. The important vorticity tilting and stretching terms play different roles in the formation process of these two counter-rotating spiral vortices. The vorticity tilting term is responsible for generating both of the spiral vortices. The vorticity stretching term acts to stretch one of the spiral vortices from the inner sphere to the outer sphere while suppressing the stretching of the other in the azimuthal direction. The different formation mechanisms for these two counter-rotating spiral vortices lead to the structure of the spiral TG vortices.

1. Introduction

The spherical Couette flow between two concentric rotating spheres usually shows dynamical behaviour analogous to the classical circular Couette flow between two concentric rotating cylinders in the equatorial regions, and to the flow between two plane

† Present address: Geophysical Institute, Graduate School of Science, Tohoku University, Aoba-Ku, Sendai, 980-8578, Japan.

rotating disks in the polar regions. Therefore, the study of this flow is of basic importance in finding a general hydrodynamic stability theory for rotating fluid in an enclosed cavity volume. Owing to the spherical geometry and rotation in this spherical shell flow situation, understanding the fluid dynamics of the motion is also relevant to both global astrophysical and geophysical processes and engineering applications.

In the spherical Couette flow system, the closed nature of the flow and its dependence on various factors lead to a wide variety of flow solutions and mechanisms from which instability arises. Most previous experimental investigations were restricted to the cases of small and medium gap widths in which the first instability occurred as Taylor vortices at the equator (e.g. Munson & Menguturk 1975; Wimmer 1976, 1981; Yavorskaya *et al.* 1980; Nakabayashi 1983; Bühler 1990; Bar-Yoseph *et al.* 1990; Egbers & Rath 1995). Some experimental and theoretical studies were also conducted recently for wide gap widths in which the first instability appeared in a form of non-axisymmetric spiral waves (Egbers & Rath 1995; Araki, Mizushima & Yanase 1997; Wulf, Egbers & Rath 1999). When the outer sphere is held stationary, with the inner sphere rotating, the spherical Couette flow between them is characterized by three control parameters: the Reynolds number, clearance ratio and rotational acceleration rate. We have carried out a series of experimental work on this concentric flow for the range of clearance ratios where the Taylor instability occurs in the equatorial region (Nakabayashi 1983; Nakabayashi & Tsuchida 1988*a*, *b*). In these studies, the Reynolds number was increased stepwise by a quasi-static increase of the rotation frequency of the inner sphere, and the final flow field of the last step was used as the initial condition for obtaining the flow at the next step. These experiments showed a similar laminar-turbulent transition to that in the circular Couette flow with only the inner cylinder rotating.

A fascinating vortex formation in spherical Couette flow with the inner sphere rotating was observed at a higher Reynolds number, and the induced vortices were called spiral Taylor–Görtler (TG) vortices by Nakabayashi (1983). In each hemisphere, this supercritical spiral TG vortex flow consists of one toroidal TG vortex near the equator and some pairs of spiral vortices in high-latitude regions whose axes are tilted with respect to the azimuthal direction. The spiral TG vortices travel in the azimuthal direction at about half of the rotational speed of the inner sphere. Although the characteristics of the spiral TG vortices were described in our previous experimental studies, the dynamical problems (i.e. detailed structure, and formation mechanism) have remained unresolved since it is difficult to obtain quantitative results simultaneously and the data obtained from the measurements are insufficient for analysis. Thus a direct numerical simulation, which can provide a reliable source of information, would be a suitable tool for a more detailed investigation of the spiral TG vortices. With a spectral method, Dumas & Leonard (1994) have successfully numerically simulated the spiral TG vortices in the spherical Couette flow between two concentric spheres with the inner sphere rotating for a narrow gap case with clearance ratio $\beta = 0.06$, and the results were in very good agreement with our previous experimental flow in the same case (Nakabayashi 1983). The inclination angle and number of spiral vortices agreed well. Dumas & Leonard (1994) first referred those vortex-splitting regions as vortex branches. As in our previous experimental result, they found six spiral cells with three corresponding 'starting points' were found in each hemisphere. Further, they suggested that the terminology 'starting points' used for describing the spiral vortices in our previous experimental work (also seen in figure 6 of Nakabayashi 1983) should be 'ending points'. We will show in the present study that their suggestion is basically correct as if one considers the formation

location of the vortex branches. For the case of both spheres rotating in spherical Couette flow, Zikanov (1996) was able to compute the spiral TG vortices by using a pseudospectral method, and his numerical results provided a detailed description of the three-dimensional flows and the pattern of transitions among various regimes. However, our knowledge about the spiral TG vortices in the spherical Couette flow is still far from complete.

The objective of the present study is to investigate through a direct numerical simulation the interesting vortex flow that we observed in our experiments. In Sha, Nakabayashi & Ueda (1998), we considered a numerical algorithm designed for three-dimensional, time-dependent incompressible Navier–Stokes fluids, and decoupling between the velocity and the pressure was achieved. The numerical method for solving the Navier–Stokes equations in spherical polar coordinates was presented in detail in that work. The numerical code, which is second-order accurate in time and space based on the finite-difference scheme, was used to compute the spherical Couette flow between two spheres with the inner sphere rotating, and we successfully simulated the subcritical flows (0-vortex flow, 0-vortex flow with pinch) and the supercritical flows (TG vortex flow, spiral TG vortex flow). In this paper, we specifically focus on the fluid dynamics of the spiral TG vortex flow for a moderate gap case with clearance ratio $\beta = 0.14$ (Nakabayashi 1983). Careful direct numerical simulation of the spiral TG vortex flow has been performed, and a systematic analysis carried out to explore the detailed structure, formation process and mechanism of the vortices.

The paper is organized as follows. In § 2, the governing equations and boundary conditions are presented first. Then the numerical formation and procedure are explained. The numerical results for the spiral TG vortex flow are presented in § 3, in which the three-dimensional spatial configuration, transient features and generation mechanism are discussed. Concluding remarks are given in § 4.

2. Mathematical formation and solution method

2.1. *Governing equations of motion*

We consider the motion of an isothermal, incompressible, Newtonian fluid contained in an annulus between two concentric spheres. The spheres are assumed to be rigid and the cavity between them is filled with a viscous fluid. The inner sphere is constrained to rotate about the vertical axis with a prescribed angular velocity Ω, while the outer sphere is fixed. The inner and outer radii of the spheres are R_1 and R_2, respectively. The Navier–Stokes equations and the continuity equation, together with appropriate initial and boundary conditions, completely describe the physics of this spherical Couette flow problem.

The incompressible Navier–Stokes equation and the continuity equation are

$$\frac{\partial \boldsymbol{u}}{\partial t} + \boldsymbol{u} \cdot \nabla \boldsymbol{u} = -\nabla p + \frac{1}{Re} \nabla^2 \boldsymbol{u}, \tag{2.1}$$

$$\nabla \cdot \boldsymbol{u} = 0, \tag{2.2}$$

respectively, where $\boldsymbol{u}$ is the velocity field, p is the kinematic pressure and Re is the Reynolds number, defined as $Re = \Omega R_1^2 / \nu$ where ν is the kinematic viscosity. The governing equations have been non-dimensionalized with the characteristic velocity scale ΩR_1 and the characteristic length scale R_1.

The above equations are now rewritten in spherical polar coordinates (r, θ, ϕ) as

follows:

$$\frac{\partial u_r}{\partial t}+\frac{1}{r^2}\frac{\partial}{\partial r}[r^2(u_r u_r)]+\frac{1}{r\sin\theta}\frac{\partial}{\partial\theta}[\sin\theta(u_\theta u_r)]+\frac{1}{r\sin\theta}\frac{\partial}{\partial\theta}[u_\phi u_r]-\frac{u_\theta u_\theta}{r}-\frac{u_\phi u_\phi}{r}$$
$$=-\frac{\partial p}{\partial r}+\frac{1}{Re}\left\{\frac{1}{r^2}\frac{\partial}{\partial r}\left(r^2\frac{\partial u_r}{\partial r}\right)+\frac{1}{r^2\sin\theta}\frac{\partial}{\partial\theta}\left(\sin\theta\frac{\partial u_r}{\partial\theta}\right)\right.$$
$$\left.+\frac{1}{r^2\sin^2\theta}\frac{\partial^2 u_r}{\partial\phi^2}-\frac{2u_r}{r^2}-\frac{2}{r^2\sin\theta}\frac{\partial(\sin\theta u_\theta)}{\partial\theta}-\frac{2}{r^2\sin\theta}\frac{\partial u_\phi}{\partial\phi}\right\}, \tag{2.3}$$

$$\frac{\partial u_\theta}{\partial t}+\frac{1}{r^2}\frac{\partial}{\partial r}[r^2(u_r u_\theta)]+\frac{1}{r\sin\theta}\frac{\partial}{\partial\theta}[\sin\theta(u_\theta u_\theta)]+\frac{1}{r\sin\theta}\frac{\partial}{\partial\phi}[u_\phi u_\theta]-\frac{u_\phi u_\phi}{r\tan\theta}+\frac{u_\theta u_r}{r}$$
$$=-\frac{1}{r}\frac{\partial p}{\partial\theta}+\frac{1}{Re}\left\{\frac{1}{r^2}\frac{\partial}{\partial r}\left(r^2\frac{\partial u_\theta}{\partial r}\right)+\frac{1}{r^2\sin\theta}\frac{\partial}{\partial\theta}\left(\sin\theta\frac{\partial u_\theta}{\partial\theta}\right)\right.$$
$$\left.+\frac{1}{r^2\sin^2\theta}\frac{\partial^2 u_\theta}{\partial\phi^2}+\frac{2}{r^2}\frac{\partial u_r}{\partial\theta}-\frac{u_\theta}{r^2\sin^2\theta}-\frac{2\cos\theta}{r^2\sin^2\theta}\frac{\partial u_\phi}{\partial\phi}\right\}, \tag{2.4}$$

$$\frac{\partial u_\phi}{\partial t}+\frac{1}{r^2}\frac{\partial}{\partial r}[r^2(u_r u_\phi)]+\frac{1}{r\sin\theta}\frac{\partial}{\partial\theta}[\sin\theta(u_\theta u_\phi)]+\frac{1}{r\sin\theta}\frac{\partial}{\partial\phi}[u_\phi u_\phi]+\frac{u_\phi u_r}{r}+\frac{u_\phi u_\theta}{r\tan\theta}$$
$$=-\frac{1}{r\sin\theta}\frac{\partial p}{\partial\phi}+\frac{1}{Re}\left\{\frac{1}{r^2}\frac{\partial}{\partial r}\left(r^2\frac{\partial u_\phi}{\partial r}\right)+\frac{1}{r^2\sin\theta}\frac{\partial}{\partial\theta}\left(\sin\theta\frac{\partial u_\phi}{\partial\theta}\right)\right.$$
$$\left.+\frac{1}{r^2\sin^2\theta}\frac{\partial^2 u_\phi}{\partial\phi^2}+\frac{2}{r^2\sin\theta}\frac{\partial u_r}{\partial\phi}+\frac{2\cos\theta}{r^2\sin^2\theta}-\frac{\partial u_\theta}{\partial\phi}-\frac{u_\phi}{r^2\sin^2\theta}\right\}, \tag{2.5}$$

$$\frac{1}{r^2}\frac{\partial}{\partial r}(r^2u_r)+\frac{1}{r\sin\theta}\frac{\partial}{\partial\theta}(\sin\theta u_\theta)+\frac{1}{r\sin\theta}\frac{\partial u_\phi}{\partial\phi}=0, \tag{2.6}$$

where u_r, u_θ and u_ϕ are the velocity components in the radial, meridional and azimuthal directions, respectively.

No-slip (rigid) boundary conditions on the spherical boundaries are

$$\left.\begin{aligned} u_r=u_\theta=0,\quad u_\phi=\sin\theta \quad \text{on} \quad r=R_1/R_1=1,\\ u_r=u_\theta=u_\phi=0 \quad \text{on} \quad r=R_2/R_1. \end{aligned}\right\} \tag{2.7}$$

2.2. *Numerical procedure*

In this subsection, the numerical procedure for solving the spherical Couette flow with the three-dimensional, time-dependent incompressible Navier–Stokes equations in spherical polar coordinates is described. Further details of this numerical method are to be found in Sha *et al.* (1998).

The governing equations of motion are discretized in space and time by a finite-difference method. Spatial discretization is carried out in the computational domain between the two concentric spheres. The spatial discrete operators are evaluated using the central finite-difference scheme on a staggered grid (Harlow & Welch 1965) and the spatial discretization is second-order accurate in space. For the time integration, we have used a semi-implicit time-advancement scheme with the implicit Crank–Nicolson second-order-accurate scheme for the conservative part of the viscous term and the explicit Adams–Bashforth second-order-accurate scheme for the convective and the remaining viscous terms. The pressure term is treated in a mixed form of the Crank–Nicolson and Adams–Bashforth scheme. However, these fully discretized equations

for the primitive variables are still coupled via the incompressibility condition, and are expensive to compute directly. Here, the decoupling between the velocity and pressure of the discretized equations is achieved by an approximate factorization method (Sha *et al.* 1998). This decoupling process leads to several smaller decoupled systems for the velocity components and the pressure, respectively, so the computational cost of calculations of the incompressible time-dependent Navier–Stokes equations in this spherical Couette flow problem can be significantly reduced in the velocity–pressure formulation. In this numerical algorithm, we introduced two intermediate velocities into the split discretized equations, and a discrete Poisson equation for the pressure could be obtained easily based on the incompressibility condition. With the approximate factorization method, the order of the temporal accuracy can be preserved. As a result, the discretization of the numerical method remains second-order accurate in time and space. The system of split discretized equations is then time-advanced to obtain the solution.

The approximate factorization technique (Beam & Warning 1976; Briley & McDonald 1977; Kim & Moin 1985) is used to treat the discrete velocity equation. The velocity is calculated by solving three tridiagonal matrices with a standard TDMA (tridiagonal-matrix algorithm) method. From the discrete Poisson equation we compute the pressure, first by application of an ADI (alternating-direction implicit) method (Peaceman & Rachford 1955), and then by solving the reduced equation with a standard TDMA method for two tridiagonal matrices and with a refined TDMA method (Temperton 1975) for a cyclic tridiagonal matrix.

In the calculation, the computational domain of the three-dimensional spherical shell is divided into a number of grids $22 \times 361 \times 91$ in the radial, meridional and azimuthal directions, respectively. The staggered grid arrangement is employed in the computation where the pressure is defined at the centre of the cell and velocity components on the cell surfaces. The grids are uniform in the meridional and azimuthal directions, while a geometric distribution is used in the radial direction to improve the resolution in the near-wall region of the spheres. The above grid spacings have been shown in Sha *et al.* (1998) to be sufficient to resolve the spherical spiral TG vortex flow. In order to ensure numerical convergence, the stability of the overall numerical method is restricted by the CFL condition. The time step is required to satisfy the stability condition of $\max\{\mathrm{CFL}\} < 1$ where $\max\{\mathrm{CFL}\}$ is the maximum value of the CFL number evaluated in the computational domain. Time integration is carried out until the steady or time-periodic state is obtained.

For the initial condition, the axisymmetric solution of the so-called 1-vortex flow (Marcus & Tuckerman 1987*a*, *b*), which was obtained in our previous numerical work (Sha *et al.* 1998), has been chosen to simulate the higher-Re spiral TG vortex flow.

3. Results and discussion

The numerical computations were performed based upon the initial condition given in § 2.2. For comparison, the moderate gap of $\beta = (R_2 - R_1)/R_1 = 0.14$ has been selected to be the same as that in our previous experiments (Nakabayashi 1983, Nakabayashi & Tsuchida 1988*a*, *b*). The Reynolds number Re was quasi-statically increased ($\mathrm{d}R^*/\mathrm{d}t = 0.0006$, where R^* is defined as $R^* = Re/Re_c$ in which Re_c is the critical Reynolds number for occurrence of the TG vortex) in order to eliminate the effect of the rotation acceleration rate on the spherical Couette flow solutions (Nakabayashi & Tsuchida 1995). As we increased Re the 1-vortex flow became unstable due to secondary instability, and its symmetry was broken. This secondary

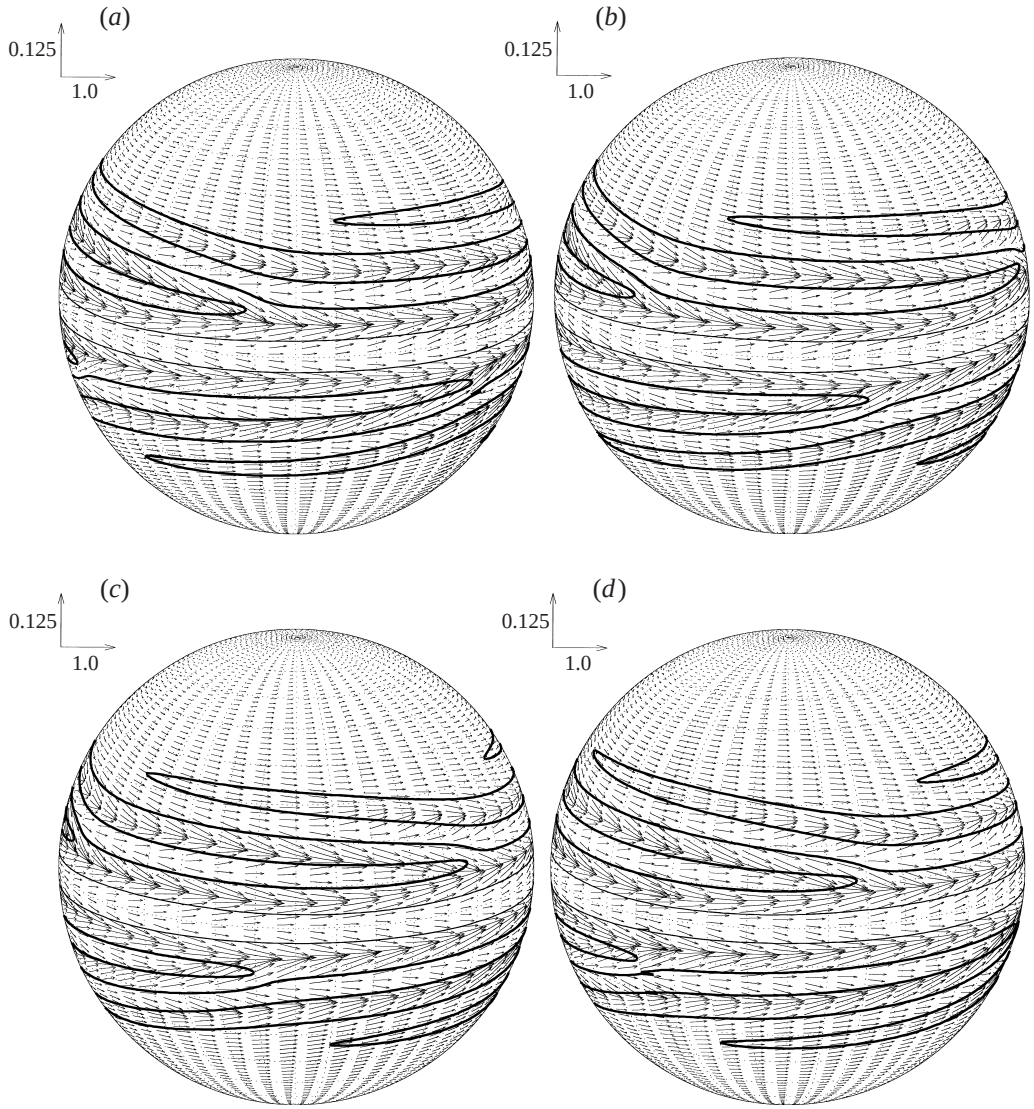

FIGURE 1. Plots of the velocity vectors from the numerical simulation of the spiral TG vortex flow in the (θ, ϕ) spherical cross-section at the radial position $r = 1 + \beta/2$ (the mid-gap radius) viewed from (*a*) $\phi = 310°$, (*b*) $\phi = 220°$, (*c*) $\phi = 130°$, (*d*) $\phi = 40°$. The Reynolds number is $Re_s = 1100$. The contour of zero radial velocity ($u_r = 0$) is drawn with thin and thick solid lines: the thin lines indicate the centre positions of the two toroidal TG vortices; the thick lines, which are counted by every two thick lines from each side of the equator, correspond to the centre lines of the spiral TG vortices.

instability resulted in a transition from the 1-vortex flow to the supercritical spiral TG vortex flow at $Re_s = 1110$ (Re_s being the Reynolds number for the occurrence of spiral TG vortices). After a non-dimensional transition time $t = 270\pi$, the flow field became steady and the spiral TG vortex flow was established. In this section, we analyse in detail the direct numerical simulation results for the spiral TG vortex flow at the mature stage $t = 270\pi$, to reveal its detailed structure, and formation mechanism.

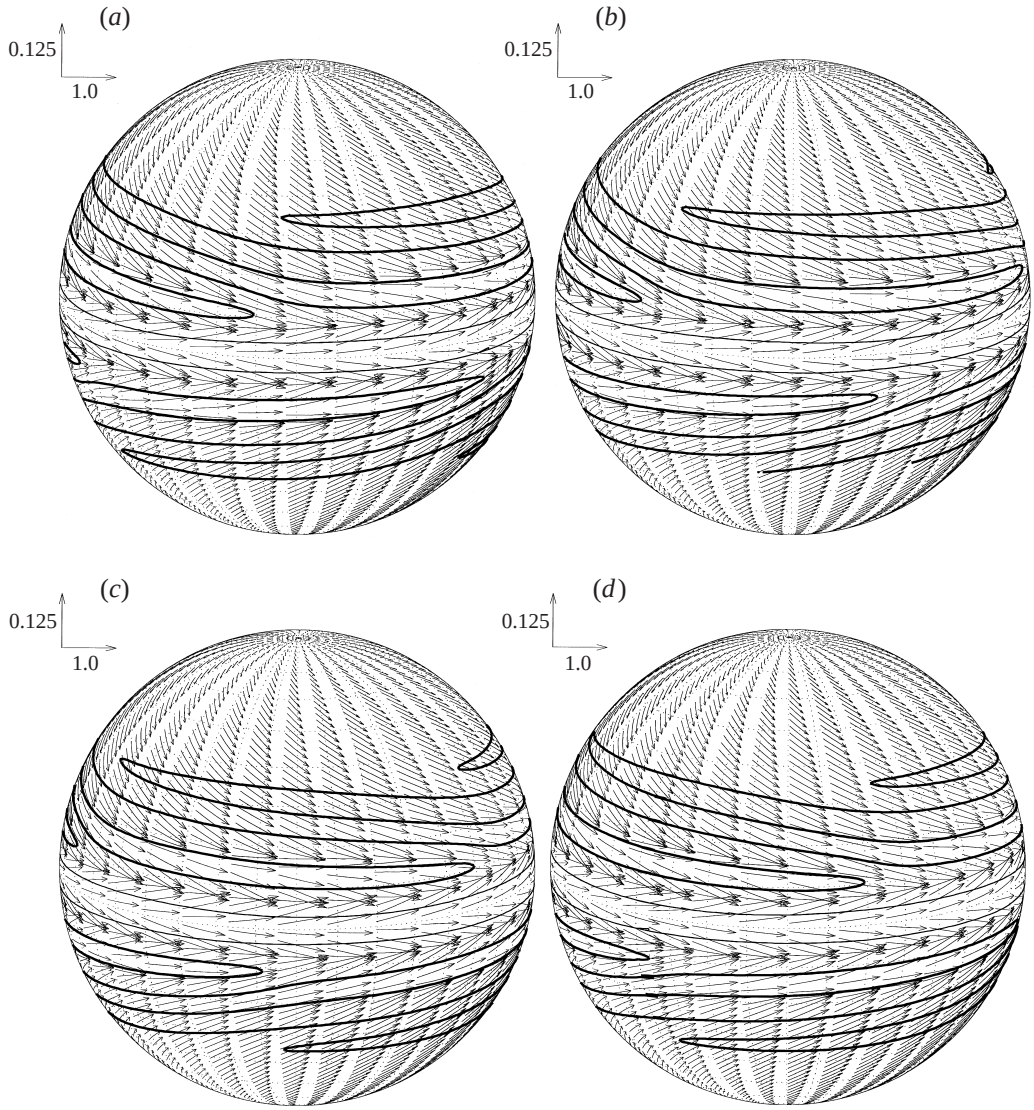

FIGURE 2. As in figure 1 but for the (θ, ϕ) spherical cross-section at the radial position $r = 1 + 0.02\beta$, representative of the spiral TG vortex flow near the inner sphere.

3.1. *Structure and features*

Figures 1, 2 and 3 show plots of the velocity vectors (u_ϕ, u_θ) of the spiral TG vortex flow solution on (θ, ϕ) spherical cross-sections at mid-gap, and near the inner and outer spheres, respectively. These figures are viewed at (*a*) $\phi = 310°$, (*b*) $\phi = 220°$, (*c*) $\phi = 130°$, (*d*) $\phi = 40°$. The pattern rotates in the same direction as the inner sphere (counterclockwise). The contours of zero radial velocity ($u_r = 0$) in these sections are drawn with thin and thick solid lines, which are the boundaries between inflow ($u_r < 0$) and outflow regions ($u_r > 0$). Thin lines indicate the centre positions of the two toroidal TG vortices. The thick ones, which are counted by every two thick lines from each side of the equator, correspond to the centre lines of the TG spiral vortices. These figures show that there exists one toroidal TG vortex and three spiral

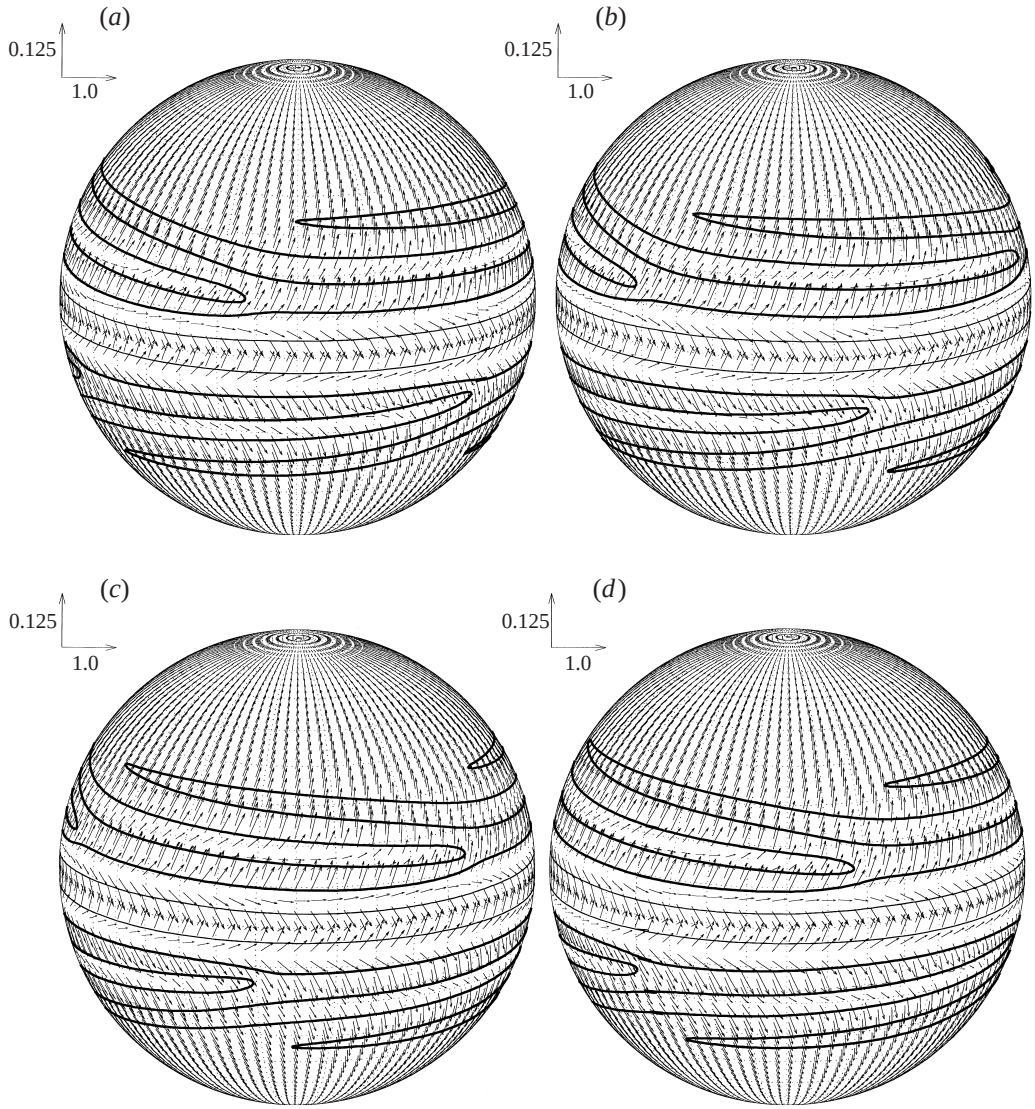

FIGURE 3. As in figure 1 but for the (θ, ϕ) spherical cross-section at the radial position $r = 1 + 0.98\beta$, representative of the spiral TG vortex flow near the outer sphere.

TG vortices in each hemisphere. The lines of the centre positions of the toroidal TG vortices are nearly parallel to the equator while the centre lines of the spiral TG vortices are inclined in the azimuthal direction. In the equatorial region where the two toroidal TG vortices are formed, the flow is divergent near the inner sphere, corresponding to inflow at the equator, while it is convergent near the outer sphere. The flow fields, portrayed in mid-latitude regions, appear to wrap the spherical cross-section with three converging/diverging zones in each hemisphere. In the regions close to the poles, the fluid flows from the poles toward the equator near the inner sphere and from the equator to the poles near the outer sphere. The particular features of the spiral TG vortex flow are of the rotational and equatorial asymmetries.

In order to gain more insight in the three-dimensional structure of the spiral TG

vortices, visualizations of the azimuthal vorticity field given by

$$\omega_\phi = \frac{1}{r}\left[\frac{\partial(ru_\theta)}{\partial r} - \frac{\partial u_r}{\partial \theta}\right] \tag{3.1}$$

are shown in figure 4. This figure can be compared with figure 6 of Dumas & Leonard (1994). Here, colour represents the azimuthal vorticity ω_ϕ iso-surfaces: purple denotes positive and yellow negative. In the spiral TG vortex flow there are one toroidal TG vortex, one toroidal vortex cell and three spiral TG vortices in each hemisphere and the flow in each hemisphere is identical except for a change of sign in ω_ϕ. So in the following we mainly focus our discussion on the northern hemisphere only. In figure 4(*d*), the toroidal TG vortex, the toroidal vortex cell A, the two spiral vortices B and C, the fore portion D another spiral vortex of the same class as C and the thin vorticity layer E adjacent to the outer sphere are indicated in the northern hemisphere. There is a toroidal vortex cell A on one side of the toroidal TG vortex, although this is not easy to deduce from the flow fields depicted in figures 1, 2 and 3. A is different from the TG vortex: they have opposite signs of circulation in the northern hemisphere, and A is connected with the spiral vortex C. Further, the TG vortex near the equator is caused by the Taylor-type first instability while A is a strengthened axisymmetric azimuthal vorticity cell in the secondary flow circulation.

Two spiral vortices B and C are observed to coexist. C is connected to the toroidal vortex cell A. The region in which C splits from A is the vortex branch reported by Dumas & Leonard (1994), and it is just the part of C which branches away from A. Vortex D is the fore portion of a vortex of the same class as the spiral vortex C at higher latitude. The spiral vortex B between the toroidal vortex cell A and the spiral vortex C forms a counter-rotating pairing with C. This spatial helical pairing forms the spiral TG vortices which were defined in our previous experiments study (Nakabayashi 1983). Thus, the spiral TG vortices are a pair of counter-rotating helical vortices. Actually, there are three pairs of these spiral vortices in each hemisphere. For each pair, a stronger, larger helical vortex (C) has as its counterpart a relatively weaker, small helical vortex (B). The spiral TG vortices are rotationally and equatorially asymmetric and travel in the same azimuthal direction as the inner rotating sphere. It is estimated that the spiral TG vortices are inclined to the azimuthal direction by an angle of approximately 4°. It can be also estimated from the simulation results that the phase speed of spiral TG vortices is about half of the inner sphere rotation speed.

The thin vorticity layer E is caused by the rapid variation of the meridional velocity near the outer spherical surface. Because of the thin vorticity layer attached to the outer sphere, it is impossible for us to see through the inside in figure 4 as it is hidden by the purple colour, i.e. the thin vorticity layer.

Figure 5 shows the azimuthal vorticity ω_ϕ at different meridional cross-sections. By tracking these vortices, more comprehensive information on the spatial configuration of the spiral TG vortices can be obtained from figure 5. We first note that the TG vortex located near the equator has a constant size and is parallel to the equator. It is also observed that the toroidal vortex cell A is either connected to the spiral vortex C or separated from C by B. Consequently, the size of A varies although its axis is nearly parallel to that of the toroidal TG vortex. An important feature in figure 5 is that the structural forms of the spiral vortices B and C are different. B, which originates at the inner sphere boundary, stretches in the gap and then extends outward into the outer-sphere boundary region, whereas the head of C disappears in the secondary flow circulation while its tail portion connects to the toroidal vortex cell

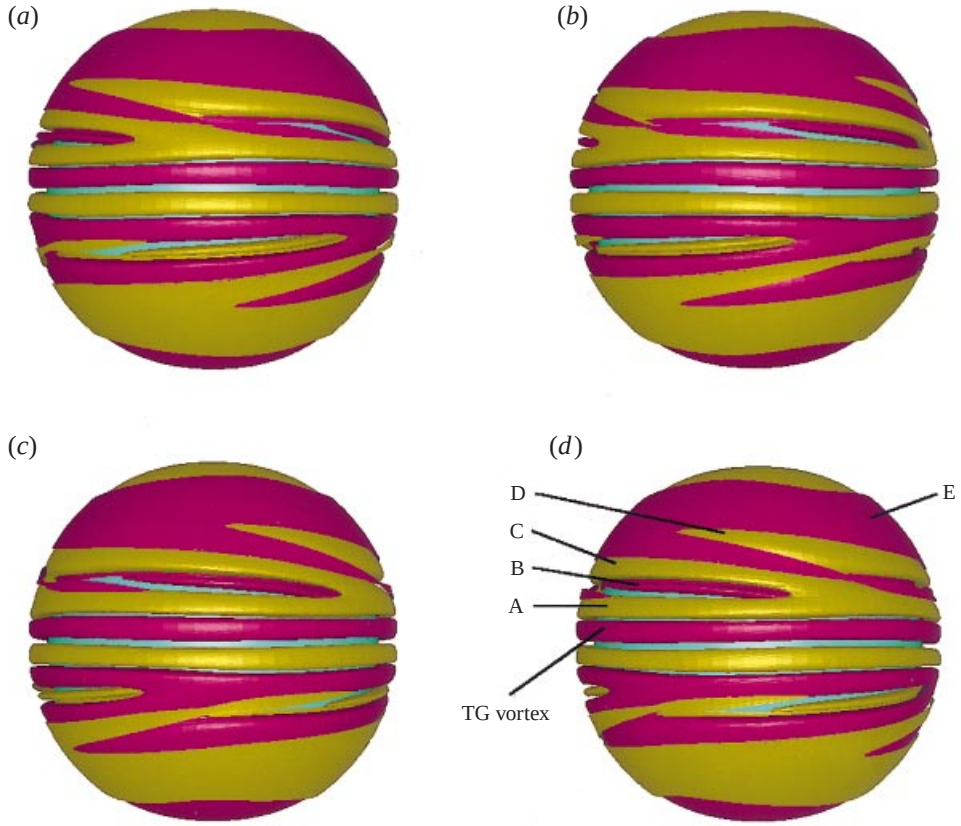

FIGURE 4. Iso-surfaces of positive and negative azimuthal vorticity components of levels ± 0.9 for the spiral TG vortex flow at $Re_s = 1110$. Purple shows a positive value and yellow a negative one. Green represents the inner sphere surface. They are viewed from the same perspectives as in figures 1, 2 and 3: (*a*) $\phi = 310°$; (*b*) $\phi = 220°$; (*c*) $\phi = 130°$; (*d*) $\phi = 40°$. 'A' denotes the toroidal vortex cell in the neighbourhood of the toroidal TG vortex. 'C' is the spiral vortex being connected with the toroidal vortex cell A. 'B' between A and C is an accompanying spiral vortex of C, and has the opposite sign of vorticity to the toroidal vortex cell A and spiral vortex C. 'D' indicates a fore portion of another spiral vortex. 'E' represents a thin vorticity layer adjacent to the outer spherical boundary.

A at lower latitude. The spiral TG vortices appear in a helical combined form of two counter-rotating spiral vortices B and C whose structures differ from one another. It is also demonstrated that thin vorticity layers are formed near both the sphere boundaries, e.g. the thin vorticity layer E is seen adjacent to the outer-sphere surface.

To obtain a clearer image of the spiral TG vortices, we subtract the 0-vortex flow solution, which was obtained in Sha *et al.* (1998), from the spiral TG vortex flow field,

FIGURE 5. Azimuthal vorticity at different meridional cross-sections of the region between $\theta = 50°$ and $\theta = 130°$ for the spiral TG vortex flow at $Re_s = 1110$. The meridional cross-sections are selected over one wavelength of the spiral TG vortices at (*a*) $\phi = 32°$, (*b*) $\phi = 52°$, (*c*) $\phi = 72°$, (*d*) $\phi = 92°$, (*e*) $\phi = 112°$, (*f*) $\phi = 132°$, (*g*) $\phi = 152°$, (*h*) $\phi = 172°$, (*i*) $\phi = 192°$. The tick marks on the inner and outer spheres are spaced at intervals of $\pi/18$ radians. The gap width has been exaggerated by trebling from the interval $[1, 1+\beta]$ to $[1, 3(1+\beta)]$. The contour levels range from -6.5 to 6.5 in steps of 0.5. Solid lines indicate the positive values while dashed lines indicate negative ones. The labels A, B, C, D and E are the same as in figure 4.

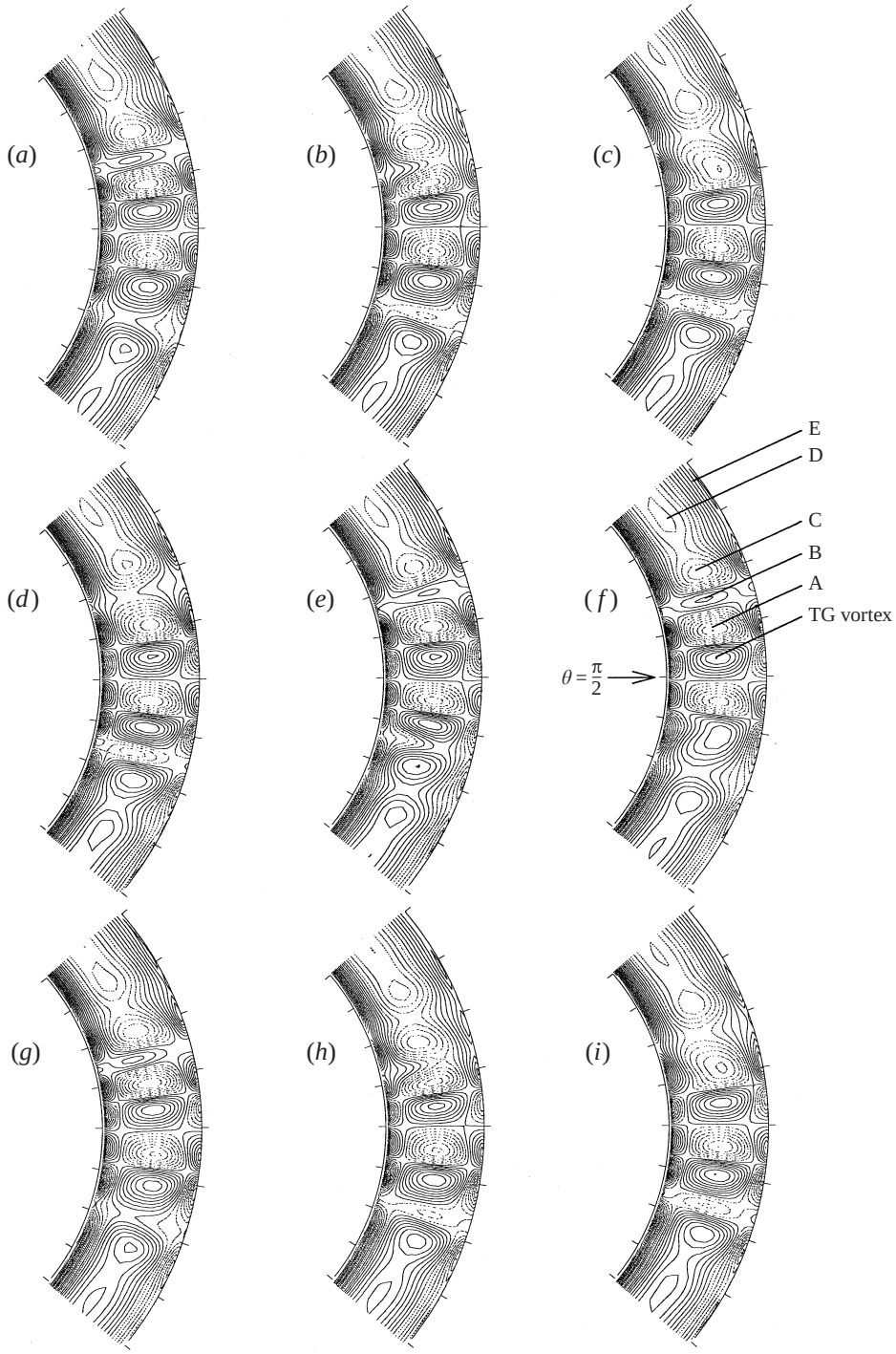

FIGURE 5. For caption see facing page.

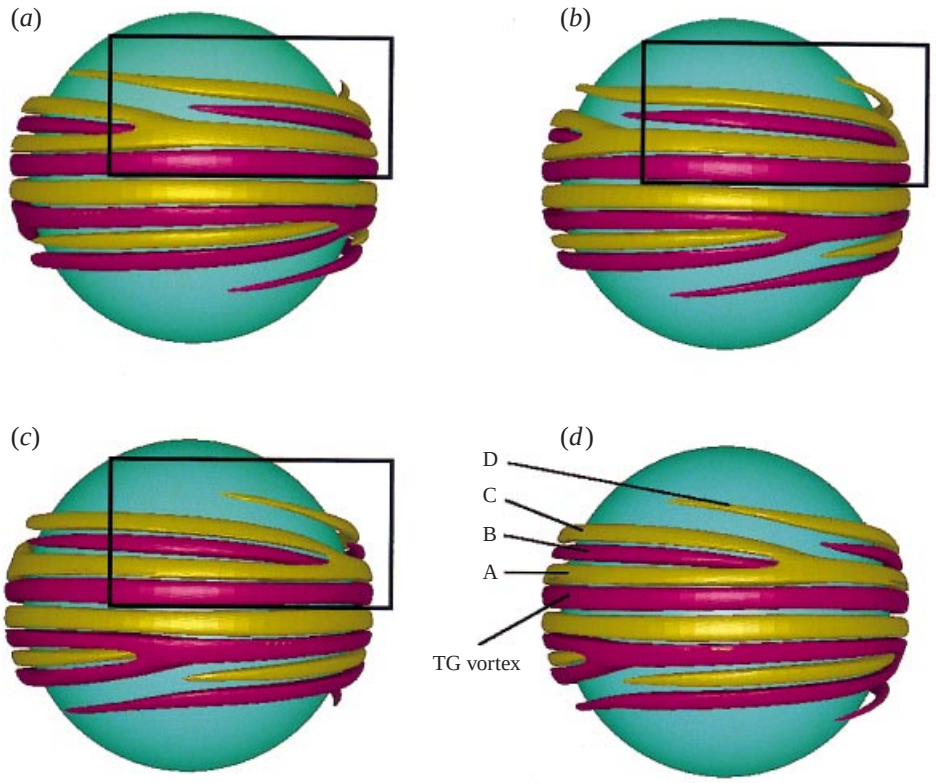

FIGURE 6. As in figure 4 but for the iso-surfaces of positive and negative azimuthal vorticity components of levels ± 0.75 for the spiral TG vortex flow field at $Re_s = 1110$ from which the 0-vortex flow solution at $Re = 800$ has been subtracted. The frames in (*a*)–(*c*) show the regions for which close-ups of the detailed structure of the spiral TG vortices is given in figure 7. The labels A, B, C and D are the same as in figure 4.

and show visualizations of the modified azimuthal vorticity field in figure 6. The thin vorticity layers, which were formed in the secondary flow circulation near the inner and outer spherical boundaries, have been erased in these figures for clarity. Figure 6 clearly shows the three-dimensional structure of the spiral TG vortices which we have described above. Further, in figure 7 we can examine more closely the detailed structure of these vortices (i.e. starting and ending points, branching region) in the three framed regions given in figure 6. Figure 7 clearly shows that the spiral vortex C begins in the secondary flow circulation at higher latitude and ends with a connection to the toroidal vortex cell A at lower latitude. In contrast, the spiral vortex B starts on the inner rotating spherical surface at lower latitude and ends on the outer stationary spherical surface at higher latitude. So, when discussing the formation location of these spiral vortices at the lower latitude the terminology 'ending point' is appropriate for describing the spiral vortex C while for the spiral vortex B 'starting point' is appropriate. This is also made more clear in next subsection as we look into the evolution process of these spiral vortices. In table 1, we summarize the characteristics of the spiral TG vortices obtained from the previous experiments (Nakabayashi 1983; Nakabayashi & Tsuchida 1988*a*) and the present numerical study. Clearly, they are in good agreement. Finally, an illustration of the three-dimensional structure of the spiral TG vortex flow in the northern hemisphere is given in figure 8.

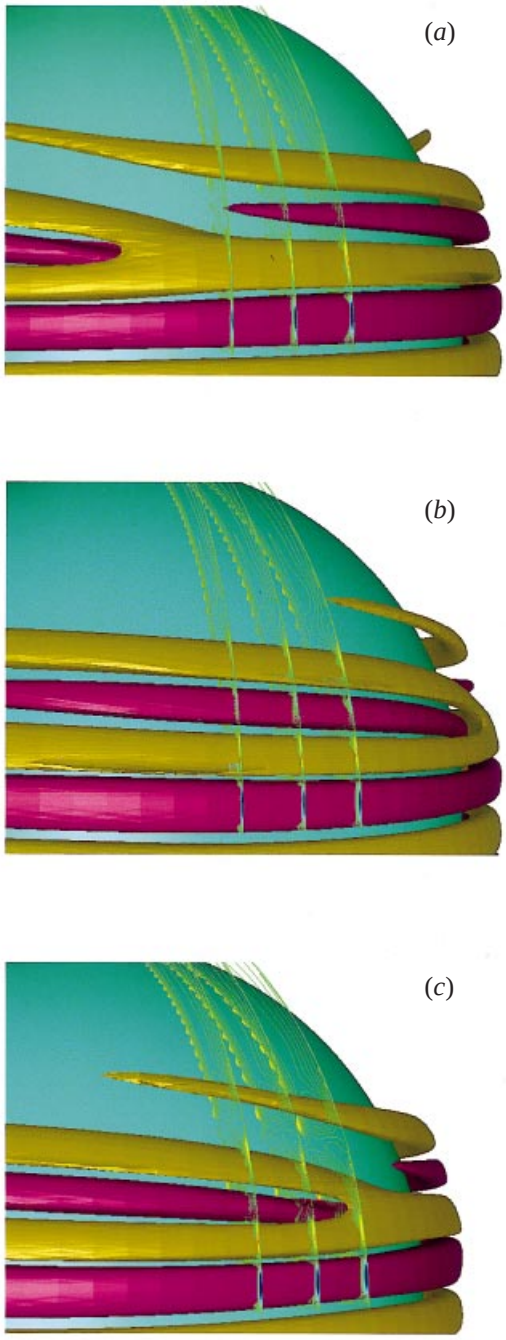

FIGURE 7. Close-up visualizations of the detailed structure of the spiral TG vortices: perspective view of iso-surfaces of the azimuthal vorticity plus three slices of the azimuthal vorticity component. Respectively, (*a*), (*b*) and (*c*) correspond to the frames in figure 6 (*a*), (*b*) and (*c*). Note in (*a*) the 'ending point' of the spiral vortex B, in (*b*) the 'starting point' of the spiral vortex C, and in (*c*) the 'starting point' of the spiral vortex B and vortex branching region. Levels of iso-surfaces of positive and negative azimuthal vorticity components are the same as in figure 6, and contour levels in the slices range from −3.0 to 3.0 in steps of 0.3.

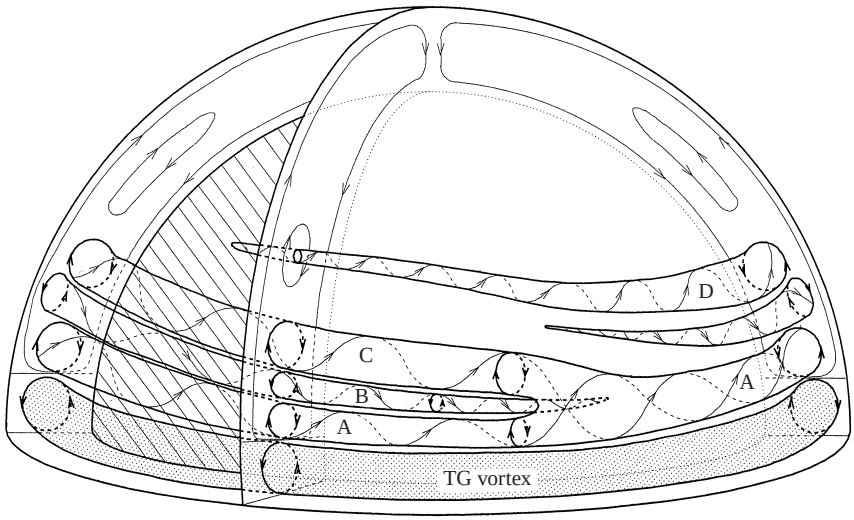

FIGURE 8. An illustration of the three-dimensional structure of the spiral TG vortex flow in the spherical Couette flow in the northern hemisphere. The outer sphere is held stationary and the inner sphere is constrained to rotate about the vertical axis. The clearance ratio β is 0.14 for a moderate gap case, and the Reynolds number Re is quasi-statically increased to obtain this supercritical vortex flow at $Re_s = 1100$. The labels A, B, C and D are the same as in figure 4.

	Dynamical characteristics	Geometrical characteristics
Previous experiments (Nakabayashi 1983; Nakabayashi & Tsuchida 1988*a*)	$R^* = 1.13$ ($Re_s = 1017$) Move in direction of rotation Phase speed about half of the inner-sphere rotation speed	Three pairs of spiral vortices in the northern hemisphere Rotational asymmetry Inclination angle 3°
Present numerical study	$R^* = 1.18$ ($Re_s = 1110$) Move in rotating direction Phase speed about half of the inner-sphere rotating speed	Three pairs of spiral vortices in each hemisphere Rotational and equatorial asymmetries Inclination angle 4°

TABLE 1. Summary of some characteristics of the spiral Taylor–Görtler (TG) vortices in the spherical Couette flow between two spheres with the inner sphere rotating and the outer sphere fixed. The clearance ratio β is 0.14 in the laboratory experiments and in this numerical study.

3.2. *Formation process*

In this subsection, we are concerned with the formation process of the spiral TG vortices and investigate the transient features. Figure 9 is a sequence of projections of the azimuthal vorticity ω_ϕ, onto the (θ, ϕ)-plane of iso-surfaces, illustrating the temporally and spatially growing structure of the spiral TG vortices. For ease of description, the dynamic evolution is considered in three stages, i.e. the initial stage in figure 9(a, b), the developing stage in figure 9(c, d), and the mature stage in figure 9(e, f).

It is seen in figure 9(a) that at $t = 108\pi$ the flow field still retains the rotational and equatorial reflection symmetries. As time progresses, the symmetries are broken. Figure 9(b), shows at a late time of the initial stage ($t = 227\pi$) that tearing begins to

occur in the vortex EC (the evolving vortex C) and the vortex EB (the evolving vortex B) appears to be formed in the inner rotating sphere boundary. At an early time of the developing stage ($t = 231\pi$) shown in figure 9(*c*), EC is tilted at an angle to the azimuthal direction and split into three parts, but EB is still attached to the inner sphere at this stage. By the late time at $t = 244\pi$ of the developing stage (see figure 9*d*), EC is elongated and it appears to be reconnected with the vortex cell EA (the evolving vortex A). At the same time EB is stretched from the inner-sphere boundary region and then extends into the outer-sphere boundary region. At an early time of the mature stage ($t = 252\pi$) shown in figure 9(*e*), EC is now completely merged with the toroidal vortex cell A. The vortex branch region, which Dumas & Leonard (1994) mentioned, is created by the connection of the spiral vortex C with the toroidal vortex cell A, and the spiral vortex B is strengthened. It is seen that the pairing process between the two counter-rotating spiral vortices B and C occurs and this results in the spiral TG vortices. This is more apparent when we look at the spiral TG vortex flow at a late time of the mature stage ($t = 270\pi$) in figure 9(*f*). We observe that the vortex tearing, splitting, tilting, reconnecting and stretching phenomena emerge in the formation of the spiral TG vortices. After the spiral TG vortex flow is completely formed in figure 9(*f*), the flow field then remains in a time-periodic state. It is clear from the above results that the pairing of two alternating helical vortices is the key process that determines the structural character of the spiral TG vortices in this spherical Couette flow.

3.3. *Formation mechanism*

To investigate the formation mechanism of the spiral TG vortex flow, we consider the vorticity production by analysing the vorticity equation. The equation for the vorticity is obtained by applying the curl operator to (2.1). This yields

$$\frac{\partial \boldsymbol{\omega}}{\partial t} + \boldsymbol{u}\cdot\nabla\boldsymbol{\omega} = \boldsymbol{\omega}\cdot\nabla\boldsymbol{u} + \frac{1}{Re}\nabla^2\boldsymbol{\omega}, \tag{3.2}$$

where $\boldsymbol{\omega} = \nabla \times \boldsymbol{u}$ is the vorticity vector. Since the spiral TG vortices are dominated by elongated quasi-streamwise vorticity structure, we consider only the azimuthal component ω_ϕ of the vorticity vector. Using the Navier–Stokes equations in spherical polar coordinates described in § 2.1, the expression for the evolution of the azimuthal vorticity from (3.2) is

$$\begin{aligned}
&\frac{\partial \omega_\phi}{\partial t} + u_r\frac{\partial \omega_\phi}{\partial r} + \frac{u_\theta}{r}\frac{\partial \omega_\phi}{\partial \theta} + \frac{u_\phi}{r\sin\theta}\frac{\partial \omega_\phi}{\partial \phi} + \frac{u_\phi\omega_r}{r} + \frac{u_\phi\omega_\theta}{r}\cot\theta \\
&\quad = \omega_r\frac{\partial u_\phi}{\partial r} + \frac{\omega_\theta}{r}\frac{\partial u_\phi}{\partial \theta} + \omega_\phi\left(\frac{1}{r\sin\theta}\frac{\partial u_\phi}{\partial \phi} + \frac{u_r}{r} + \frac{u_\theta}{r}\cot\theta\right) \\
&\qquad + \frac{1}{Re}\left\{\frac{1}{r^2}\frac{\partial}{\partial r}\left(r^2\frac{\partial \omega_\phi}{\partial r}\right) + \frac{1}{r^2\sin\theta}\frac{\partial}{\partial \theta}\left(\sin\theta\frac{\partial \omega_\phi}{\partial \theta}\right)\right. \\
&\qquad \left. + \frac{1}{r^2\sin^2\theta}\frac{\partial^2\omega_\phi}{\partial \phi^2} + \frac{2}{r^2\sin\theta}\frac{\partial \omega_r}{\partial \phi} + \frac{2\cos\theta}{r^2\sin^2\theta}\frac{\partial \omega_\theta}{\partial \phi} - \frac{\omega_\phi}{r^2\sin^2\theta}\right\},
\end{aligned} \tag{3.3}$$

where ω_r, ω_θ are vorticity components in the radial direction and in the meridional direction, respectively. The second term on the left-hand side of (3.3) is the vorticity advection term. The first, second and third terms on the right-hand side are the production rate terms representing the effects of vorticity tilting, twisting and stretching, respectively. The last term on the right-hand side is the vorticity viscous diffusion

term. Next, we calculate the size of each term to determine which are important to the formation of the spiral TG vortices.

The time evolution of (θ, ϕ)-plane distributions of the quantities in (3.3), namely, (*a*) the azimuthal vorticity component, (*b*) the vorticity tilting term, (*c*) the vorticity stretching term, (*d*) the vorticity twisting term, (*e*) the vorticity advection term and (*f*) the vorticity viscous diffusion term is illustrated in figures 10–13. As in figure 9, these figures are projected onto the (θ, ϕ)-plane in Cartesian coordinates and depicted over the range of $0^\circ \leqslant \phi \leqslant 360^\circ$ and $50^\circ \leqslant \theta \leqslant 130^\circ$. First, the result at $t = 108\pi$ is shown in figure 10 for reference. Then, figures 11, 12 and 13 give the results for the representative initial stage at $t = 227\pi$, developing stage at $t = 244\pi$ and mature stage at $t = 270\pi$, respectively. For convenience of discussion, all the above quantities have been integrated along the radial direction over the gap. In these figures, solid lines denote positive values while dashed lines represent negative ones.

In figure 10 at $t = 108\pi$, the distributions of all quantities are still axisymmetric and reflection symmetric. In this equilibrium flow state, the vorticity stretching term is much smaller than other terms, and the vorticity tilting, twisting, advection and viscous diffusion terms mainly balance each other. A close inspection of (*d*) the vorticity twisting term, (*e*) the vorticity advection term and (*f*) the vorticity viscous diffusion term in figures 11, 12 and 13 shows that the vorticity advection term advects the vorticity downstream in the azimuthal direction. Second, we see that the vorticity viscous diffusion term always tends to cause attenuation of the vorticity. Third, we find that the vorticity twisting term, which is basically cancelled out by the vorticity tilting term and acts here in the same manner as the vorticity viscous diffusion term, usually acts to decrease the vorticity. We restrict ourselves in the following to examining the transient changes of (*a*) the azimuthal vorticity component, (*b*) the vorticity tilting term and (*c*) the vorticity stretching term in figures 11, 12 and 13.

In the initial stage at $t = 227\pi$ shown in figure 11, the 1-vortex flow becomes unstable due to the secondary instability which results in a transition to the supercritical spiral TG vortex flow at $Re_s = 1110$. It is known that it takes quite a long time for the transition from the equilibrium flow state to the spiral TG vortex flow to occur. It is seen in figure 11 that the symmetries have been broken at this time. As we are mainly concerned with spiral vortex formation, we will limit our examination to the high-latitude regions in the northern hemisphere where the spiral vortices B and C are generated. It is observed in figure 11(*b*) that the distribution pattern of the vorticity tilting term tends to be inclined in the azimuthal direction and there are positive and negative peaks, consistent with the locations of the positive-sign vorticity (spiral vortex B) and negative-sign vorticity (spiral vortex C) shown in figure 11(*a*). But, on comparing figures 11(*c*) and 11(*a*), it is easily seen that the locations of peaks of the vorticity stretching term do not match those of the spiral vortices B and C, implying that at this time the vorticity stretching term has little effect on the formation of the spiral TG vortices. This means that at the initial stage, the vorticity tilting term is the only dominant contribution and is particularly responsible

FIGURE 9. Time sequences of a plane view of the iso-surfaces of positive and negative azimuthal vorticity components of levels ± 0.75 for illustrating the evolution process of the spiral TG vortex flow at $Re_s = 1110$. (*a*) $t = 108\pi$, (*b*) $t = 227\pi$, (*c*) $t = 231\pi$, (*d*) $t = 244\pi$, (*e*) $t = 252\pi$, (*f*) $t = 270\pi$. They are projected onto the (θ, ϕ)-plane in Cartesian coordinates and visualized in a frame of $0^\circ \leqslant \phi \leqslant 360^\circ$ and $50^\circ \leqslant \theta \leqslant 130^\circ$. Purple shows positive values and yellow negative values. The labels A, B and C are the same as in figure 4. The labels EA, EB and EC mean evolving into vortex A, evolving into B and evolving into C, respectively.

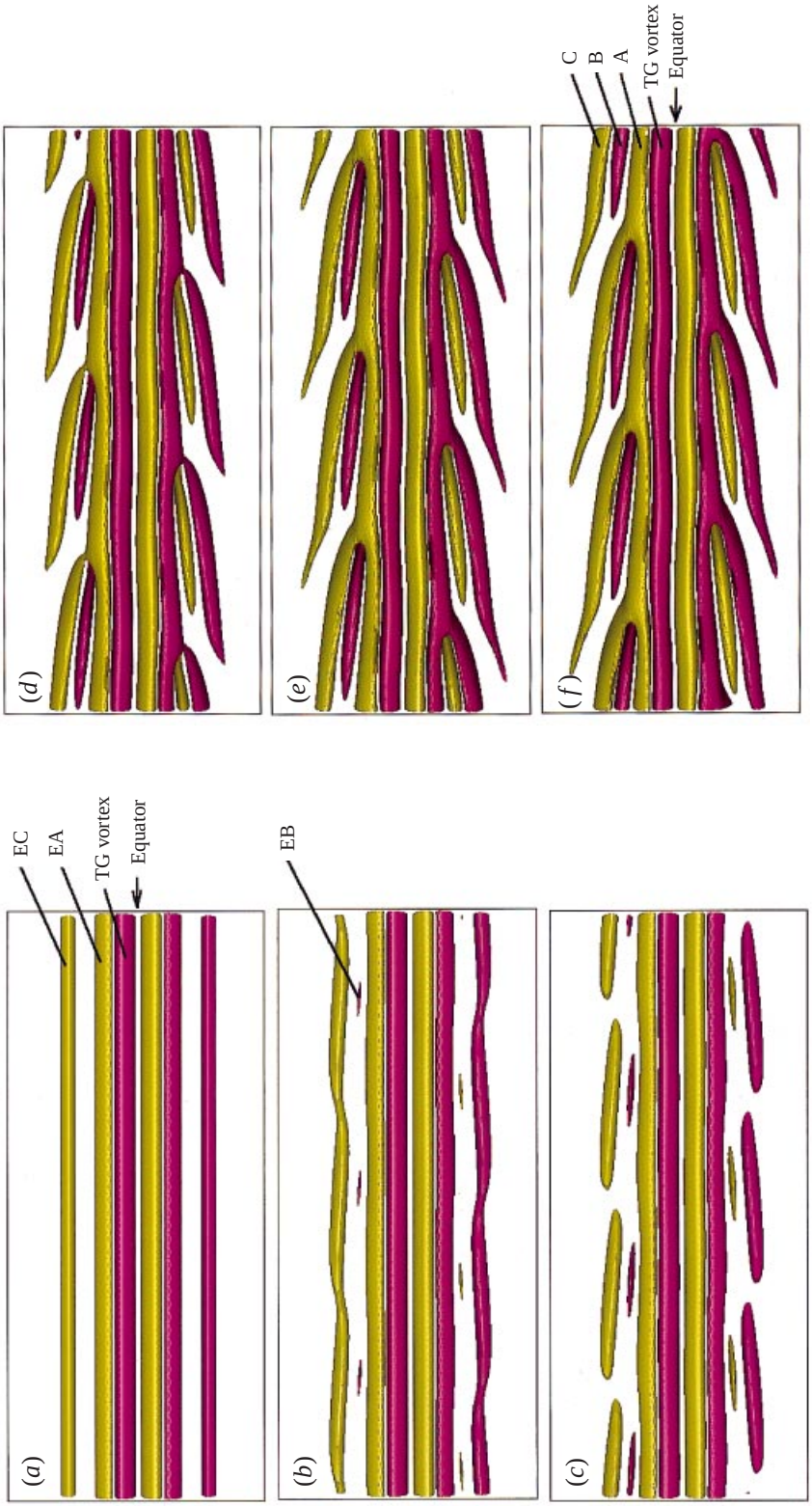

FIGURE 9. For caption see facing page.

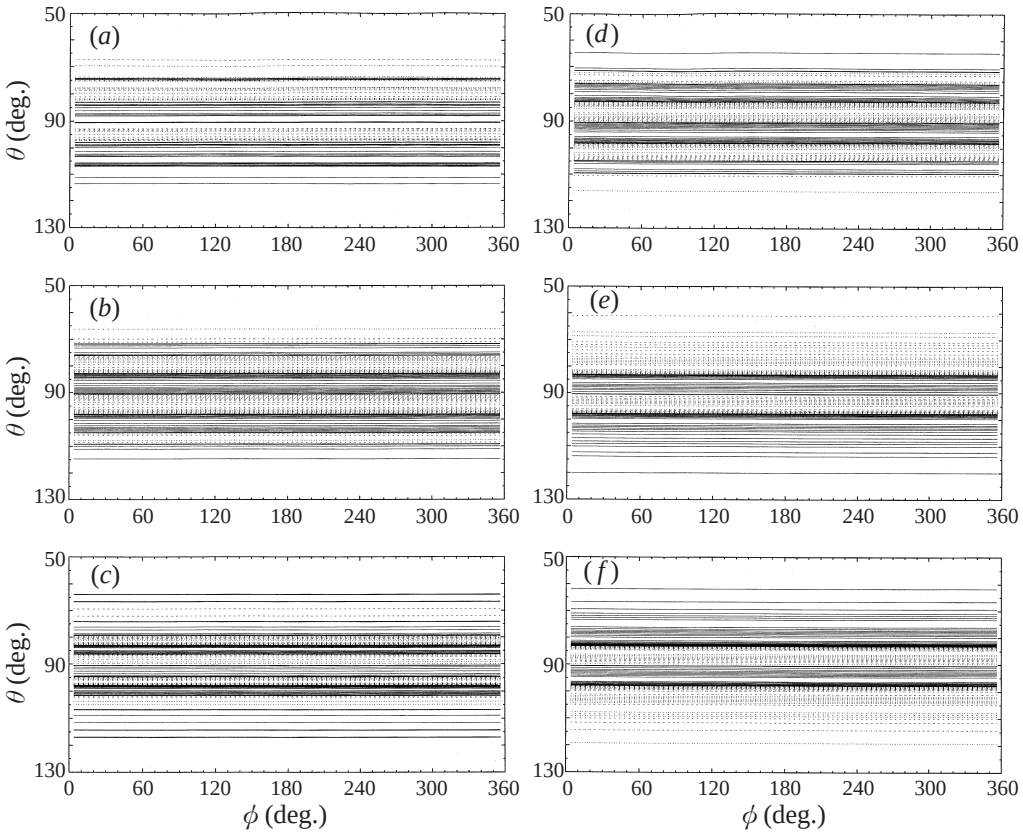

FIGURE 10. (θ, ϕ)-plane distributions of each quantity in the azimuthal vorticity equation at $t = 108\pi$: (*a*) the azimuthal vorticity component represented by contour lines at the levels $0, \pm 0.03, \pm 0.06, \pm 0.09, \pm 0.095, \pm 0.105, \pm 0.11, \pm 0.115, \pm 0.12, \pm 0.15, \pm 0.18$; (*b*) the vorticity tilting term, the contour levels range from -3.0 to 3.0 in steps of 0.3; (*c*) the vorticity stretching term, the contour levels range from -0.01 to 0.01 in steps of 0.001; (*d*) the vorticity twisting term, the contour levels range from -3.0 to 3.0 in steps of 0.3; (*e*) the vorticity advection term, the contour levels range from -0.3 to 0.3 in steps of 0.03; (*f*) the vorticity viscous diffusion term, the contour levels range from -0.5 to 0.5 in steps of 0.05. All quantities are integrated along the radial direction over the gap. Solid lines show positive values while dashed lines show negative ones.

for generating the spiral vortices B and C. For the developing stage at $t = 244\pi$, it is seen in figure 12(a, b) that the vorticity tilting term continues to contribute to the vorticity generation and the spiral vortices B and C are being intensified compared with the initial stage. Meanwhile, by examining closely figure 12(a, c), we find that the locations of the positive peaks of the vorticity stretching term match those of the positive-sign vorticity (spiral vortex B) and negative-sign vorticity (spiral vortex C) simultaneously. This suggests that the effect of the vorticity stretching term is to stretch the spiral vortex B from the inner sphere to the outer sphere while it suppresses the stretching of the spiral vortex C in the azimuthal direction. The vorticity stretching term becomes significant at the developing stage and plays different roles (stretching or compressing) in the evolution process of the spiral TG vortices, i.e. in the formation of the spiral vortex B and the spiral vortex C. For the formation mechanism of the spiral TG vortices at the mature stage $t = 270\pi$ shown in figure 13, the vorticity tilting term and the vorticity stretching term act in a similar manner

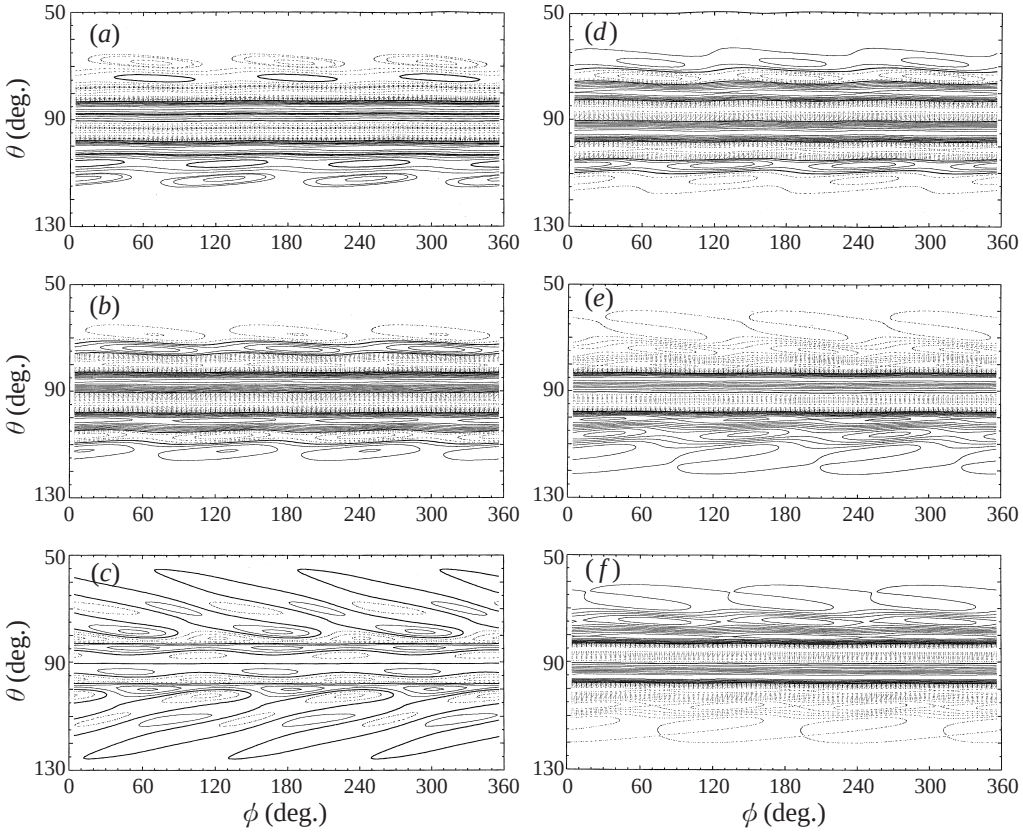

FIGURE 11. As in figure 10 but for the representative initial stage at $t = 227\pi$. Also note that the contour levels for the vorticity stretching term (c) are changed to range from -0.04 to 0.04 in steps of 0.004.

as they did at the developing stage although the two terms have been strengthened. The vorticity tilting term is responsible for maintaining the spiral TG vortices (i.e. both B and C). The vorticity stretching term provides the stretching effect on B and is responsible for maintaining it, while the vorticity stretching term also contributes to the suppression of the stretching of C. The different generation mechanisms for formation of B and C lead to the three-dimensional unique structure of the spiral TG vortices obtained in previous sections.

4. Concluding remarks

A direct numerical simulation of the flow between an inner rotating and an outer stationary sphere was conducted to investigate the detailed structure, and formation process and mechanism of the spiral Taylor–Görtler (TG) vortices. A numerical method, which is exactly second-order accurate in time and space based on the finite-difference scheme, was used to solve the Navier–Stokes equations in spherical polar coordinates. For comparison with our previous experimental work, the moderate gap case with clearance ratio $\beta = 0.14$ was chosen in the present numerical study. The axisymmetric solution of the 1-vortex flow was used as the initial condition, and the Reynolds number was quasi-statically increased to eliminate the effect of the rotational

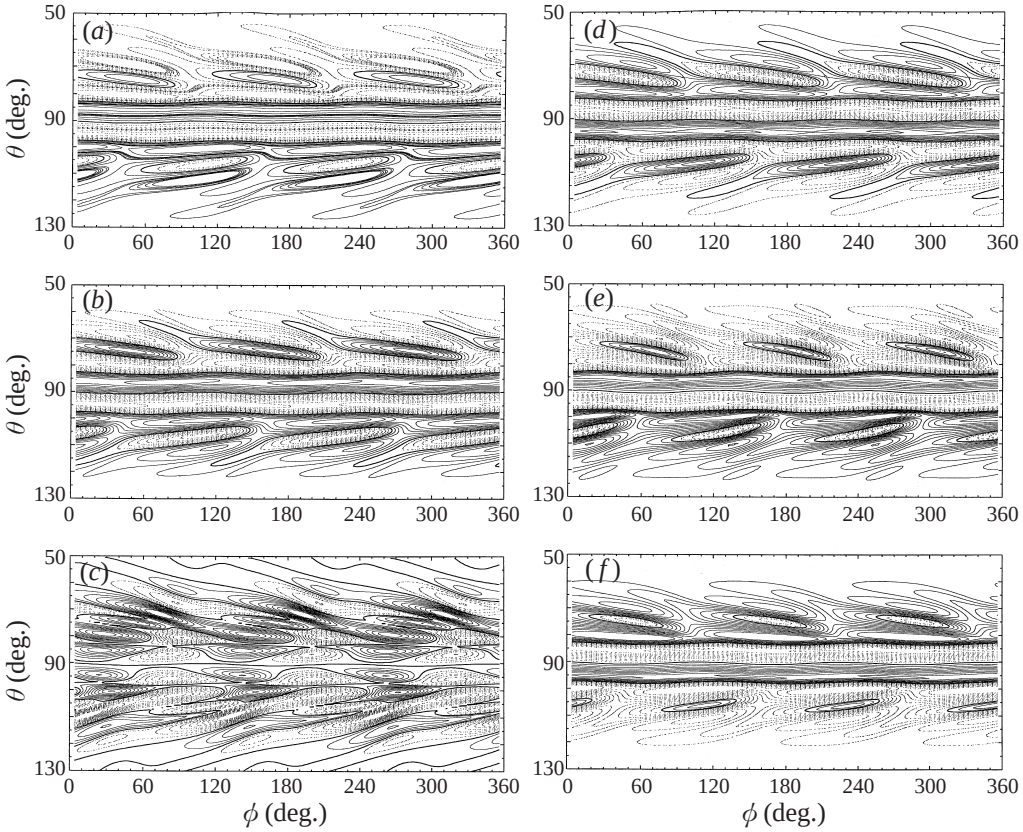

FIGURE 12. As in figure 11 but for the representative developing stage at $t = 244\pi$.

acceleration rate. With adequate initial and boundary conditions, we sucessfully simulated the supercritical spiral TG vortex flow in this spherical Couette flow.

By systematically analysing the direct numerical simulation results, we have revealed the detailed structure and features of the spiral TG vortices. It is seen that the spiral TG vortex flow consists of one toroidal TG vortex, one toroidal vortex cell, three spiral TG vortices and a secondary flow circulation in each hemisphere and this supercritical flow solution features rotational and equatorial asymmetries. Alongside the toroidal TG vortex near the equator there is a toroidal vortex cell with a sign of circulation opposite to the toroidal TG vortex. It was found that the spiral TG vortices are made up of a pair of counter-rotating, unequal spiral vortices. The spiral vortices in each pair coexist in higher latitude regions. Further, the structural forms of these two spiral vortices are different. That is, the former begins in the secondary flow circulation at higher latitude and ends with a connection to the toroidal vortex cell at lower latitude. On the other hand, the latter starts on the inner rotating spherical surface at lower latitude and ends on the outer stationary spherical surface at higher latitude. The spiral TG vortices are dominated by elongated quasi-streamwise vorticity structure and are inclined to the azimuthal direction at a small angle. It is demonstrated that the spiral TG vortices propagate in the azimuthal direction at about half of the inner sphere's rotating speed.

We showed a time sequence of visualizations of iso-surfaces of the azimuthal vorticity component to illustrate the temporally and spatially growing structure of

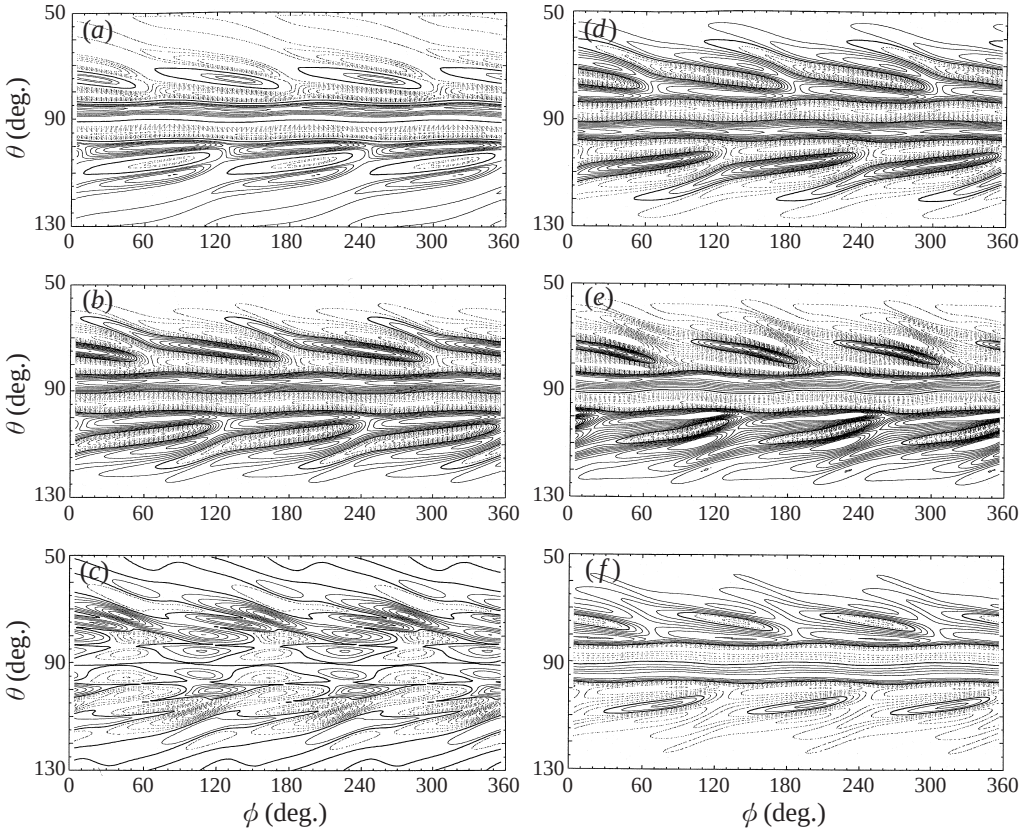

FIGURE 13. As in figure 10 but for the representative mature stage at $t = 270\pi$. In addition, the azimuthal vorticity component in (*a*) is represented by contour lines at the levels of $0, \pm 0.09, \pm 0.11, \pm 0.13, \pm 0.15, \pm 0.17, \pm 0.19, \pm 0.21, \pm 0.23, \pm 0.25, \pm 0.27$. The contour levels for the vorticity stretching term in (*c*) range from -0.1 to 0.1 in steps of 0.01 and the ones for the vorticity viscous diffusion term in (*f*) range from -1.0 to 1.0 in steps of 0.1.

the spiral TG vortices. We considered their evolution process in three stages, i.e. initial, developing and mature stages. At an early time of the initial stage, the flow field still has rotational and equatorial symmetries, but at a later time of the initial stage, vorticity tearing occurs and opposite-sign vorticity forms in the inner rotating sphere boundary. The rotational and equatorial reflection symmetries of the flow fields are broken. Early in developing stage, the vorticity torn at the initial stage is tilted with an inclination angle to the azimuthal direction and is split into three parts, while the vorticity formed in the inner rotating sphere boundary at the initial stage is still attached to the inner rotating sphere surface at this stage. Later in the developing stage, the torn, split vorticity is then elongated, tilted and appears to be reconnected with the toroidal vortex cell. At the same time, the vorticity attached to the inner sphere surface is now stretched from the inner-sphere boundary region and extends into the outer-sphere boundary region. At the mature stage, the reconnection is completed and the vortex branch region is created. The pairing process between the two counter-rotating spiral vortices is finished and this results in the spiral TG vortices. Vortex tearing, splitting, tilting, reconnecting, stretching and compressing occur in the formation of the spiral vortices. The pairing of two alternating helical vortices is the key process in the evolution of the spiral TG vortices.

To clarify the formation mechanism of the spiral TG vortices, the terms in the azimuthal vorticity component equation were calculated at the different evolving stages. It was shown that the vorticity advection term acts to advect the vorticity downstream in the azimuthal direction and the vorticity viscous diffusion term always tends to attenuate the vorticity. The vorticity twisting term, which behaves similarly to the vorticity viscous diffusion term, usually decreases the vorticity. However, the remaining vorticity tilting and stretching terms are important in formation of the spiral TG vortices. These two terms play different roles in the process of forming two counter-rotating spiral vortices. It was found at the initial stage that the effect of the vorticity stretching term is negligible, and the vorticity tilting term is the dominant contribution and is responsible for generating both of the spiral vortices at this initial stage. At the developing and mature stages, the vorticity tilting term still generates vorticity in the spiral vortices. It works to tilt the spiral vortices at an angle to the azimuthal direction. However, the vorticity stretching term has the effect of stretching one of the spiral vortices from the inner sphere to the outer sphere while also suppressing the stretching of the other spiral vortex in the azimuthal direction. These different mechanisms combine to create the structure of the spiral TG vortices in this spherical Couette flow.

We are grateful to the reviewers for their useful comments and suggestions which helped to improve the paper. Appreciation is given to Professor H. Ueda, Disaster Prevention Research Institute, Kyoto University for his support during the study. Thanks is given to Dr W. Grace and Dr R. Brown for their help, and also to Mr K. Hattori and Mr K. Hidaka for their valuable assistance. The work was partially supported by the Grants-in-Aid for Scientific Research from the Ministry of Education, Science and Culture, Japan. The computations were carried out on the NEC supercomputer (SX4) at the computing center of the National Institute for Environmental Studies, Japan.

REFERENCES

Araki, K., Mizushima, J. & Yanase, S. 1997 The nonaxisymmetric instability of the wide-gap spherical Couette flow. *Phys. Fluids* **9**, 1197–1199.

Bar-Yoseph, P., Solan, A., Hillen, R. & Roesner, K. G. 1990 Taylor vortex flow between eccentric coaxial rotating spheres. *Phys. Fluids* A **2**, 1564–1573.

Beam, R. M. & Warming, R. F. 1976 An implicit finite-difference algorithm for hyperbolic system in conservation-law form. *J. Comput. Phys.* **22**, 87–110.

Briley, W. R. & McDonald, H. 1977 Solution of the multidimensional compressible Navier–Stokes equations by a generalized implicit method. *J. Comput. Phys.* **24**, 372–397.

Bühler, K. 1990 Symmetric and asymmetric Taylor vortex flow in spherical gaps. *Acta Mech.* **81**, 3–38.

Dumas, G. & Leonard, A. 1994 A divergence-free spectral expansions method for three-dimensional flows in spherical-gap geometries. *J. Comput. Phys.* **111**, 205–219.

Egbers, C. & Rath, H. J. 1995 The existence of Taylor vortices and wide-gap instabilities in spherical Couette flow. *Acta Mech.* **111**, 125–140.

Harlow, F. H. & Welch, J. E. 1965 Numerical calculation of time-dependent viscous incompressible flow of fluid with free surface. *Phys. Fluids* **8**, 2182–2189.

Kim, J. & Moin, P. 1985 Application of a fractional-step method to incompressible Navier–Stokes equations. *J. Comput. Phys.* **59**, 308–323.

Marcus, P. S. & Tuckerman, L. S. 1987*a* Simulation of flow between concentric rotating spheres. Part 1. Steady states. *J. Fluid Mech.* **185**, 1–30.

Marcus, P. S. & Tuckerman, L. S. 1987*b* Simulation of flow between concentric rotating spheres. Part 2. Transition. *J. Fluid Mech.* **185**, 31–65.

Munson, B. R. & Menguturk, M. 1975 Viscous incompressible flow between concentric rotating spheres. Part 3. Linear stability and experiments. *J. Fluid Mech.* **69**, 705–719.

Nakabayashi, K. 1983 Transition of Taylor–Görtler vortex flow in spherical Couette flow *J. Fluid Mech.* **132**, 209–230.

Nakabayashi, K. & Tsuchida, Y. 1988*a* Spectral study of the laminar–turbulent transition in spherical Couette flow. *J. Fluid Mech.* **194**, 101–132.

Nakabayashi, K. & Tsuchida, Y. 1988*b* Modulated and unmodulated travelling azimuthal waves on the toroidal vortices in a spherical Couette system. *J. Fluid Mech.* **195**, 495–522.

Nakabayashi, K. & Tsuchida, Y. 1995 Flow-history effect on higher modes in the spherical Couette system. *J. Fluid Mech.* **295**, 43–60.

Peaceman, D. W. & Rachford, H. H. 1955 The numerical solution of parabolic and elliptic differential equations. *J. Soc. Indust. Appl. Maths* **3**, 28–41.

Sha, W., Nakabayashi, K. & Ueda, H. 1998 An accurate second-order approximation factorization method for time-dependent incompressible Navier–Stokes equations in spherical polar coordinates. *J. Comput. Phys.* **142**, 47–66.

Temperton, C. J. 1975 Algorithms for the solution of cyclic tridiagonal systems. *J. Comput. Phys.* **19**, 317–323.

Wimmer, M. 1976 Experiments on a viscous fluid flow between concentric rotating spheres. *J. Fluid Mech.* **78**, 317–335.

Wimmer, M. 1981 Experiments on the stability of viscous flow between two concentric rotating spheres. *J. Fluid Mech.* **103**, 117–131.

Wulf, P., Egbers, C. & Rath, H. J. 1999 Routes to chaos in wide gap spherical Couette flow. *Phys. Fluids* **11**, 1359–1372.

Yavorskaya, I. M., Belyaev, Yu. N., Monakhov, A. A., Astaf'eva, N. M., Scherbakov, S. A. & Vvedenskaya, N. D. 1980 Stability, non-uniqueness and transition to turbulence in the flow between two rotating spheres. *Rep.* 595. Space Research Institute of the Academy of Science. USSR.

Zikanov, O. Yu. 1996 Symmetry-breaking bifurcations in spherical Couette flow. *J. Fluid Mech.* **310**, 293–324.